Computing Light Masks in Neutral Atom Lithography

Jürgen Braun [a], Carsten Burstedde [b], Angela Kunoth [a]

[a] *Institut für Numerische Simulation, Universität Bonn, Wegelerstr. 6, 53115 Bonn, Germany, Phone +49–228–733144, Fax +49–228–733381*
`{braun,kunoth}@ins.uni-bonn.de`

[b] *Institute for Computational Engineering and Sciences, The University of Texas at Austin, 1 University Station, C0200, Austin, Texas 78712, USA*
`carsten@ices.utexas.edu`

Abstract

In neutral atom lithography, a collimated beam of atoms is sent through a region of standing light waves created by interfering laser beams. The intensity distribution of the light field modulates the density distribution of the atoms transversal to the beam direction. The atomic beam materializes on a substrate, and the atoms are deposited in a pattern which mimics the intensity distribution of the light. It is thus possible to create nanostructures by a suitable adjustment of the light field. While the computation of the pattern of atoms generated by any given setup of laser beams with known amplitudes and phases is straightforward, the inverse problem of deducting the appropriate amplitude and phase of each single beam to create a prescribed pattern has to our knowledge not yet been addressed.

We propose a numerical method to derive these values for a fixed setup of laser beams. We consider first the general case of unrelated beam directions and then specialize to setups which induce periodic patterns. The solution of the inverse problem is a two-step process: We use Fourier techniques to compute a set of characteristic amplitude values which enter the right hand side of a nonlinear system of equations. This system is then solved iteratively by a coordinate descent method.

Key words: Atom lithography, nanostructures, light masks, nonlinear inverse problem, Fourier transform.
2000 MSC: 65T50, 78M25, 78A60.

1 Introduction

Neutral atom lithography is a method in atomic nanofabrication to generate structures by the modulation of atomic beams with optical dipole forces. This

has become possible by the combination of laser cooling and atom optics. The control of the transversal intensity distribution of the atoms permits the deposition of atomic patterns at the nanometer scale. In contrast to classical lithography, where light is sent through thin films and masks for projection on a substrate, here the roles of light and matter are in a way interchanged. The light field takes the role of an immaterial mask. Atoms are sent through a two-dimensional region of standing light waves, whose intensity distribution is transformed to an atomic image on a substrate. An overview on this topic can be found in [11, 15].

The basic concept of neutral atom lithography can be summarized as follows: An atomic beam is collimated by transversal laser cooling and then passes through an area of standing light waves created by the superposition of laser beams. When the frequency of the laser is near an atomic resonance, optical dipole forces arise. These tend to push the atoms towards local intensity maxima for red detuned light, and towards local minima for blue detuned light. For a detailed analysis of this effect, see e. g. [9, 12, 14]. Hence, after passing through the light field, the density distribution of the atoms orthogonal to the beam direction is altered by the inhomogeneous intensity distribution of the light field. Finally, all atoms condense on the surface of a substrate. After chemical postprocessing of the substrate, the density distribution of the atoms is materialized.

The simplest way of correlating the light intensity with the atom density would be an affine-linear dependence with constant positive (red-detuned) or negative (blue-detuned) slope. However, the trajectory of each atom through the light field depends on several parameters in a rather complex way. For example, the distance of the light field to the substrate, the absolute value of its intensity, the velocity of the atoms, the thickness of the optical lense (i.e., the diameter of the laser beams), and frequency and line width of the atomic resonance all play a role in this interaction. An important notion in this context is the so-called channeling regime, where the atoms are unable to cross the potential walls of the light field. The interplay between the physical parameters mentioned above is subject to many theoretical and experimental studies (see e.g. [1,7,11] and the references therein). Though a linear dependence is hard to achieve, experiments show that it is possible to make the maxima and minima of the atom distribution correspond to the maxima and minima of the light field (for red, or vice versa for blue detuning).

While the characteristics of the atomic density profile on the substrate are subject to experimental conditions, the wave form of a coherent laser beam is generally sinusoidal. A well-defined mathematical question is thus to ask for an appropriate setup of laser beams, given a target light intensity pattern (obviously including target maxima and minima). The structure of these maxima and minima can then be replicated on the substrate by the lithography process described above. The type of functional dependence of the atom pattern

on the light intensity may be adressed seperately and afterwards by designing appropriate experimental conditions. We focus here on the mathematical question which is substantial to all experimental steps which may follow to further refine the result.

A practical strategy to generate the light field determined by the mathematical process to be described in this paper is to first split one laser beam with a specific frequency into multiple beams and let them interference afterward with different directions and phases. This can be done by holographic elements, which are capable of simultaneously diffracting an incoming laser beam into multiple beams that may be very narrowly spaced [12]. As the construction of such holographic elements is rather complicated, an a priori investigation of the required beam characteristics is necessary. These characteristics can be identified as the number of beams as well as the direction, phase and amplitude of each individual beam. The problem arising in this context is the determination of a beam setup that produces a pattern on the substrate with a prescribed structure. We consider here the case of a fixed number of beams with given directions. This corresponds to the situation of a given physical setup with installed beam splitters, and that amplitudes and phases can be influenced by filters. Likewise when using a holographic crystal, it may not be practicable to change the beam setup itself, although a continuous selection of directions is theoretically possible. The remaining degrees of freedom are thus the amplitudes and phases of the single beams.

The fundamental problem discussed here can hence be formulated as follows: Given a specific target pattern, find the amplitudes and phases for an array of N laser beams with default directions, to induce an intensity pattern on the substrate which matches this pattern or approximates it sufficiently well.

The structure of this paper is the following. After introducing the mathematical basics for the intensity distribution of the standing light waves in Section 2, we formulate the arising nonlinear inverse problem in Section 3 and provide a characterization of the given wave vectors. The ansatz for the numerical solution of the inverse problem will be a Fourier decomposition. For this reason, we introduce in Section 3.2.1 the discrete Fourier transform and review some basic properties. Since for general choices of wave vectors the discrete Fourier transform does not directly apply, as the original problem is continuous, we propose a method that interpolates the values of the coefficients in the continuous setting from the values of the discrete Fourier transform on a grid. This is first done in one dimension and extended to two dimensions by a tensor product ansatz (Section 3.2.2 and Section 3.2.3). In Section 3.3, we specialize to a class of wave vectors corresponding to periodic patterns which directly delivers the discrete information by proper scaling. The final step of the reconstruction consists in the solution of an over-determined, highly nonlinear problem for the complex coefficients, containing phase and amplitude of the single laser beams as unknowns. A least-squares ansatz leads to a cost
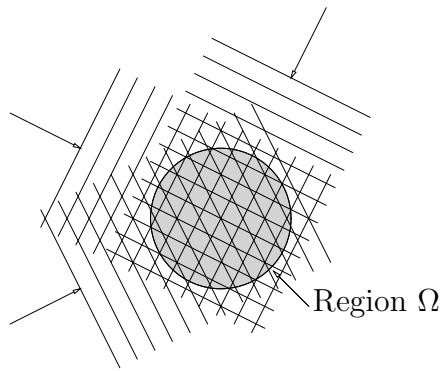
Fig. 1. Schematic view of the interfering light waves. The arrows indicate the directions of propagation of the individual waves, and the parallel lines symbolize the wave fronts. They interfere with each other in the region Ω, which is drawn as a circle for illustrative purposes. The atomic beam passes this region perpendicular to the paper plane.

functional which is minimized by a coordinate descent method in Section 3.4. Additionally, we apply the Nelder and Mead simplex method for minimization in the periodic case. In Section 4, we present numerical results for both classes of beam setups, and a selection of different patterns and the reconstructions computed with our method.

2 Mathematical Basics

We begin with the mathematical formulation of the problem, which is derived from the physical situation. Figure 1 schematically displays a laser setup. The plain light waves interfere in a region $\Omega \subset \mathbb{R}^2$, where the prescribed pattern has to be approximated. The N single waves with index $j \in I := \{1, \ldots, N\}$ are conveniently modeled as complex-valued functions $y_j(\mathbf{x}, t; \mathbf{k}_j, a_j, \varphi_j)$. The real part can be interpreted as the electric field. Its value at a given space point $\mathbf{x} \in \Omega$ and time t depends on three parameters: the direction of propagation $\mathbf{k}_j \in \mathbb{R}^2$ (the *wave vector*), the *amplitude* $a_j \in \mathbb{R}_{\geq 0}$ and the *phase* $\varphi_j \in [0, 2\pi)$. Thus, a single wave is of the form

$$y_j(\mathbf{x}, t; \mathbf{k}_j, a_j, \varphi_j) = a_j \exp\Big(\mathrm{i}\left(\langle \mathbf{k}_j, \mathbf{x}\rangle + \varphi_j - \omega t\right)\Big)$$
$$= c_j \exp\left(\mathrm{i}\langle \mathbf{k}_j, \mathbf{x}\rangle\right) \exp\left(-\mathrm{i}\omega t\right)$$

with complex-valued coefficients

$$c_j := a_j \exp\left(\mathrm{i}\varphi_j\right) .$$

Here the angular frequency ω is fixed by the properties of the laser. By $\langle \cdot, \cdot \rangle$ we denote the Euclidean inner product in $\mathbb{R}^2$. Each wave can be adjusted to an individual amplitude and phase. The direction of each beam is fixed by

the experimental setup, and its modulus is a constant because of the fixed frequency of the laser, i.e., $|\mathbf{k}_j| = K = \frac{\omega}{c}$, where c denotes the speed of light. In the remainder of the paper, we denote by

$$\mathcal{K} := \left\{ \mathbf{k}_j \in S_K^1 \ : \ j \in \mathcal{I} := \{1, \dots, N\}; \ \mathbf{k}_j \neq \mathbf{k}_l \text{ for } j \neq l \right\} \tag{1}$$

the set of all N wave vectors. The superposition of N waves is just the sum of the single functions y_j,

$$y(\mathbf{x}, t) = \sum_{j=1}^{N} y_j(\mathbf{x}, t) = \sum_{j=1}^{N} c_j \exp\left(\mathrm{i}\langle \mathbf{k}_j, \mathbf{x}\rangle\right) \exp(-\mathrm{i}\omega t).$$

Setting

$$\tilde{y}(\mathbf{x}) := \sum_{j=1}^{N} c_j \exp\left(\mathrm{i}\langle \mathbf{k}_j, \mathbf{x}\rangle\right), \tag{2}$$

y can be decomposed in space and time according to $y(\mathbf{x}, t) = \tilde{y}(\mathbf{x}) \exp(-\mathrm{i}\omega t)$. According to the physical model, the created pattern is equivalent to the intensity of the electric field, namely,

$$f_N(\mathbf{x}) = |y(\mathbf{x})|^2 = |\tilde{y}(\mathbf{x})|^2 = \left| \sum_{j=1}^{N} c_j \exp\left(\mathrm{i}\langle \mathbf{k}_j, \mathbf{x}\rangle\right) \right|^2, \quad \mathbf{x} \in \Omega. \tag{3}$$

This function can easily be evaluated, if the number of beams N, the directions $\mathbf{k}_j$ and the coefficients c_j are known. It directly relates to the chemical pattern which manifests on the substrate, which is our quantity of interest.

3   The Inverse Problem

In contrast to the easy task of evaluating the function f_N for given parameters N, $\mathbf{k}_j$ and c_j, we devote our further studies to the inverse problem, namely the computation of the coefficients c_j. From now on, we denote by f an arbitrary but fixed pattern. We aim at the approximation of the given function f by the intensity realized with N beams of appropriate amplitude and phase. This means that a function f_* has to be found with

$$f_* = \arg\min_{g \in \mathcal{S}_N} \|g - f\|_{\Omega} \tag{4}$$

over the space

$$\mathcal{S}_N = \mathcal{S}_N(\mathbf{k}_1, \dots, \mathbf{k}_N) := \left\{ g = \left| \sum_{j=1}^{N} c_j \exp\left(\mathrm{i}\langle \mathbf{k}_j, \cdot\rangle\right) \right|^2 \ : \ c_j \in \mathbb{C} \right\}, \tag{5}$$

where the involved norm $\|\cdot\|_{\Omega}$ still has to be chosen in accordance with the physical requirements. The so defined space contains all physically realizable

patterns under the parameters N and $\mathbf{k}_j \in \mathcal{K}$, $j \in \mathcal{I}$. The degrees of freedom in the space $\mathcal{S}_N$ are the complex coefficients c_j.

Remark 3.1. $\mathcal{S}_N$ is a nonlinear space over the variables c_j. The sum of two elements is generally not an element of $\mathcal{S}_N$; the set of solutions can, therefore, not be easily decomposed.

3.1 Characterization of Wave Vectors

The nonlinearity caused by the square in expansion (3) is much easier to understand if the elements of $\mathcal{S}_N$ are written in a slightly different form which hides the square and the modulus.

For a detailed analysis, it is therefore convenient to expand the sum in (3) yielding

$$f_N(\mathbf{x}) = \sum_{j=1}^{N} |c_j|^2 + \sum_{\substack{j,l=1 \\ j<l}}^{N} \left(c_j \bar{c}_l \exp\left(i\langle \mathbf{k}_{j,l}, \mathbf{x}\rangle\right) + \text{c. c.} \right) \tag{6}$$

where c. c. denotes the complex conjugate of the previous term, and the differences of wave vectors are denoted by $\mathbf{k}_{j,l} := \mathbf{k}_j - \mathbf{k}_l$. They will play a key role for the whole procedure, as they correspond to the basis vectors of the pattern in k-space. At this point, one has to distinguish two elementary cases: we separate the set

$$\mathcal{K}_{\mathrm{d}} := \{\mathbf{k}_{j,l} = \mathbf{k}_j - \mathbf{k}_l \ : \ \mathbf{k}_j, \mathbf{k}_l \in \mathcal{K} \ ; \ j,l = 1, \ldots, N \ ; \ j \neq l\} \tag{7}$$

of all possible differences into the two disjoint sets

$$\mathcal{K}_{\mathrm{d},1} := \{\mathbf{k}_{j,l} \in \mathcal{K}_{\mathrm{d}} \ : \ \mathbf{k}_{j,l} \neq \mathbf{k}_{m,n} \text{ for all } (m,n) \neq (j,l)\} \tag{8}$$

and

$$\mathcal{K}_{\mathrm{d},2} := \{\mathbf{k}_{j,l} \in \mathcal{K}_{\mathrm{d}} \ : \ \mathbf{k}_{j,l} = \mathbf{k}_{m,n} \text{ for } (m,n) \neq (j,l)\} \ . \tag{9}$$

It holds that $\mathcal{K}_{\mathrm{d}} = \mathcal{K}_{\mathrm{d},1} \cup \mathcal{K}_{\mathrm{d},2}$, and each element in $\mathcal{K}_{\mathrm{d},2}$ appears twice by different combinations of indices. In order to get rid of this redundancy, we discard each duplicate in $\mathcal{K}_{\mathrm{d},2}$ and keep in mind that to each combination of indices (j,k) there exists exactly one matching combination (m,n) with $\mathbf{k}_{j,l} = \mathbf{k}_{m,n}$. This situation is depicted in Figure 2.

The first set of wave vectors in $\mathcal{K}_{\mathrm{d},1}$ does not affect the expansion (6). When the second set $\mathcal{K}_{\mathrm{d},2}$ is not empty, the contained wave vectors lead to a redundancy as the same plane wave appears twice in the expansion (6). Mathematically, the vectors from $\mathcal{K}_{\mathrm{d},2}$ lead to pairs of linearly dependent objects. A general expansion of (3) in terms of completely linearly independent basis functions
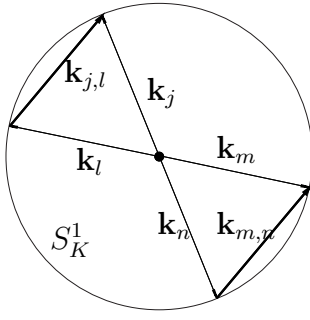
Fig. 2. The picture shows two elements $\mathbf{k}_{j,l} := \mathbf{k}_j - \mathbf{k}_l$ and $\mathbf{k}_{m,n} := \mathbf{k}_m - \mathbf{k}_l$ of the set $\mathcal{K}_{\mathrm{d},2}$ before the duplicates were discarded. One can see directly that each element in $\mathcal{K}_{\mathrm{d},2}$ appears exactly twice.

is thus given by

$$f_N(\mathbf{x}) = \sum_{j=1}^N |c_j|^2 + \sum_{\mathbf{k}_{j,l} \in \mathcal{K}_{\mathrm{d},1}} \left(c_j \bar{c}_l \exp\left(i\langle \mathbf{k}_{j,l}, \mathbf{x}\rangle\right)\right)$$
$$+ \sum_{\mathbf{k}_{j,l} \in \mathcal{K}_{\mathrm{d},2}} \left((c_j \bar{c}_l + c_m \bar{c}_n) \exp\left(i\langle \mathbf{k}_{j,l}, \mathbf{x}\rangle\right)\right), \tag{10}$$

where the indices m, n are to be understood in the sense of (9).

3.2 Fourier Analysis for General Wave Vectors

As we deal with linear combinations of plane waves, it appears natural to employ a Fourier decomposition. The two-dimensional continuous Fourier transform of (10) is composed of Dirac δ-distributions in $\mathbf{k}$-space: One peak appears at the origin and one for each term in the second and third sum, i.e.,

$$\widehat{f}_N(\mathbf{k}) = \mathcal{F}[\,f_N\,](\mathbf{k}) = \sum_{j=1}^N |c_j|^2\, \delta(\mathbf{k} - \mathbf{0}) + \sum_{\mathbf{k}_{j,l} \in \mathcal{K}_{\mathrm{d},1}} \left(c_j \bar{c}_l\, \delta(\mathbf{k} - \mathbf{k}_{j,l})\right)$$
$$+ \sum_{\mathbf{k}_{j,l} \in \mathcal{K}_{\mathrm{d},2}} \left((c_j \bar{c}_l + c_m \bar{c}_n)\, \delta(\mathbf{k} - \mathbf{k}_{j,l})\right). \tag{11}$$

Under the assumption that $\widehat{f}_N(\mathbf{k})$ is composed of δ-peaks as well whose coefficients $C(\widehat{f}_N(\mathbf{k}))$ are known for all $\mathbf{k} \in \mathcal{K}_{\mathrm{d}}$, the complex numbers c_j are the unknowns of a system of nonlinear equations, which is written as

$$C(\widehat{f}_N(\mathbf{k}_{j,l})) = \begin{cases} c_j \bar{c}_l & \text{if } \mathbf{k}_{j,l} \in \mathcal{K}_{\mathrm{d},1} \\ c_j \bar{c}_l + c_m \bar{c}_n & \text{if } \mathbf{k}_{j,l} \in \mathcal{K}_{\mathrm{d},2} \\ \sum_{j=1}^N |c_j|^2 & \text{if } \mathbf{k}_{j,l} = 0 \end{cases} \tag{12}$$

for all $\mathbf{k}_{j,l} \in \mathcal{K}_{\mathrm{d}}$.

For numerical calculations however, we need to resort to the discrete version of the continuous Fourier transform. This poses the problem that, in general, the coefficient exactly at $\mathbf{k}_{j,l}$ cannot be inferred directly from the discrete Fourier transform, as $\mathbf{k}_{j,l}$ is most probably located somewhere *between* the grid points in the discrete $\mathbf{k}$-space.

We will now shortly review the connections between the discrete and continuous Fourier transform.

3.2.1 Discrete and Continuous Fourier Transform

We will formulate the connections between the discrete and continuous Fourier transform on the basis of the one-dimensional case. The generalization to higher dimensions is straightforward and completely analogous.

Let $g : \mathbb{R} \to \mathbb{C}$ be a continuous function. We will only consider function values over $x \in [0, q)$, so strictly speaking, it needs to be defined and continuous only on this interval. The value q characterizes the size of the *observation window*. This range is sampled equidistantly with a resolution $L \in \mathbb{N}$. The grid points and the associated function values are defined as

$$x_j = q\frac{j}{L}, \qquad g_j = g(x_j), \qquad j = 0, \ldots, L-1. \tag{13}$$

The discrete Fourier transform of g is given by

$$\widehat{g}_l = \frac{1}{L} \sum_{j=0}^{L-1} g_j \exp\left(-2\pi i \frac{jl}{L}\right), \qquad l = 0, \ldots, L-1, \tag{14}$$

and its inversion formula reads

$$g_j = \sum_{l=0}^{L-1} \widehat{g}_l \exp\left(2\pi i \frac{jl}{L}\right). \tag{15}$$

Note that we have periodicity $g_j = g_{j+L}$. To establish the symmetry to the sampling of function values in space, we search a continuous function $\widehat{g}(k)$ defined on $k \in [0, p)$, where p is left unspecified for the moment, which is also sampled equidistantly,

$$k_l = p\frac{l}{L}, \qquad \widehat{g}_l = \widehat{g}(k_l). \tag{16}$$

Due to the periodicity, the window of definition of $\widehat{g}$ and the indices l can be shifted arbitrarily, as long as the cardinality is exactly L. In our case, it is most convenient to use the symmetric window $k \in [\frac{p}{2}, \frac{p}{2})$. By inserting the definitions of x_j and k_l into (14), we can identify a suitable choice for p,

$$pq = 2\pi L \quad \Longleftrightarrow \quad \widehat{g}(k) = \frac{1}{L} \sum_{j=0}^{L-1} g(x_j) \exp(-ikx_j). \tag{17}$$

8

In the limit $L \to \infty$, which transforms the sum into an integral, $\widehat{g}(k_l)$ converges to the classical definition of the l-th coefficient in the Fourier series for q-periodic functions.

3.2.2 Reconstruction of Subgrid Information

When only the values $\widehat{g}_l$ of the discrete Fourier transformation are available (14) as usual in numerical applications, one needs to interpolate the values of $\widehat{g}(k)$ from (17) for certain values of $k_i^{\mathrm{d}} \in \mathcal{K}_{\mathrm{d}}^1$, $i \in \mathcal{I}_{\mathrm{d}}^1$, which may lie between the sampling points k_l. To suppress interference of multiple wave vectors, we require that each cell between the grid points may only contain one such entry, which is equivalent to requiring

$$k_{\min} \geq \frac{p}{L} = \frac{2\pi}{q} \quad \Longleftrightarrow \quad q \geq \lambda_{\max} = \frac{2\pi}{k_{\min}} \, . \tag{18}$$

Here we have introduced a maximum wavelength $\lambda_{\max}$ corresponding to the minimal distance in the set $\mathcal{K}_{\mathrm{d}}^1$ defined by

$$k_{\min} = \min\{|k_i^{\mathrm{d}} - k_j^{\mathrm{d}}| \; : \; i,j \in \mathcal{I}_{\mathrm{d}}^1, i \neq j\} \, . \tag{19}$$

Remark 3.2. Condition (18) agrees with the physically obvious rule that the frequency information can only be recovered if the window of observation contains at least one full wavelength. This requirement is independent of the sampling resolution L.

Consider a function of the form

$$g(x) = c \, \exp(\mathrm{i}kx) \tag{20}$$

for which we only know $k \in \mathcal{K}_{\mathrm{d}}^1$ and the values of the discrete Fourier transform $\widehat{g}_l$ for a given observation window q and resolution L. The aim is to reconstruct the value of its amplitude c. If incidentally $k = k_l$ for some $l \in \{0, \ldots, L-1\}$, the trivial solution is $c = \widehat{g}_l$. Most probably, however, k lies between two grid points. We denote these by k_- and k_+, according to

$$k_- < k < k_+ \, , \qquad k_- + \tilde{b}_0 := k =: k_+ - \tilde{b}_1 \, , \qquad \tilde{b}_0 + \tilde{b}_1 = \frac{p}{L} = \frac{2\pi}{q} \, . \tag{21}$$

Note that $\tilde{b}_0$ and $\tilde{b}_1$ are independent of L. The value of the Fourier transform immediately on the left of k is given by

$$\widehat{g}_- := \widehat{g}(k_-) = \frac{c}{L} \sum_{j=0}^{L-1} \exp\left(\mathrm{i}kx_j\right) \exp\left(-\mathrm{i}k_- x_j\right)$$

$$= \frac{c}{L} \sum_{j=0}^{L-1} \exp\left(\mathrm{i}\frac{q}{L}\tilde{b}_0 j\right) =: c \cdot \rho \exp(\mathrm{i}\eta) \, .$$

The functions $\rho(\tilde{b}_0) \geq 0$ and $\eta(\tilde{b}_0) \geq 0$ can be derived by geometric arguments according to

$$\rho = \frac{1}{L} \sin\left(\frac{q}{2}\tilde{b}_0\right) \sin\left(\frac{q}{2}\frac{\tilde{b}_0}{L}\right)^{-1}, \qquad \eta = \frac{q}{2}\,\tilde{b}_0\left(1 - \frac{1}{L}\right).$$

A similar result holds for $\hat{g}_+ := \hat{g}(k_+)$. In the limit $L \to \infty$, we use the identity $\lim_{x\to 0} \sin(x) \to x$ and obtain

$$\hat{g}_- = c\,\mathrm{sinc}(b_0)\exp(i\pi b_0)\,, \tag{22a}$$
$$\hat{g}_+ = c\,\mathrm{sinc}(b_1)\exp(-i\pi b_1)\,, \tag{22b}$$

with the usual definition $\mathrm{sinc}(x) := \sin(\pi x)/(\pi x)$ and the scaling

$$b_0 := \frac{q}{2\pi}\tilde{b}_0\,, \qquad b_1 := \frac{q}{2\pi}\tilde{b}_1\,. \tag{23}$$

Note that this is equivalent to the transformation to a grid with unit spacing because of $b_0 + b_1 = \frac{q}{2\pi}(\tilde{b}_0 + \tilde{b}_1) = 1$.

¿From (22), we can now separately derive the absolute value and the argument of c. The argument can be derived as

$$\arg(c) = \arg(\hat{g}_-) - \pi b_0 = \arg(\hat{g}_+) + \pi b_1\,. \tag{24}$$

Likewise, its amplitude can be determined as

$$|c| = |\hat{g}_-/\mathrm{sinc}(b_0)| = |\hat{g}_+/\mathrm{sinc}(b_1)|\,. \tag{25}$$

Remark 3.3 (Discretization errors). Since the limit $L \to \infty$ cannot be reached in reality, these relations hold only approximately. As a consequence, an averaging process between the solutions obtained from $\hat{g}_-$ and $\hat{g}_+$ needs to be implemented which accounts for small deviations in the complex numbers involved.

Remark 3.4 (Required resolution). The size of the observation window q is arbitrary, under the condition that (18) is fulfilled. To be able to capture all possible values of k, the maximum difference has to be contained in the symmetric window in k-space,

$$k_{\mathrm{max}} < \frac{p}{2} \qquad \Longleftrightarrow \qquad L > \frac{q k_{\mathrm{max}}}{\pi} \tag{26}$$

with

$$k_{\mathrm{max}} = \max\{|k_i^{\mathrm{d}} - k_j^{\mathrm{d}}| \; : \; i, j \in \mathcal{I}_{\mathrm{d}}^1, i \neq j\}\,.$$

This enforces a certain minimum resolution L. Combining (18) with (26), we obtain

$$L \geq 2\frac{k_{\mathrm{max}}}{k_{\mathrm{min}}}\,. \tag{27}$$

10

The minimal resolution necessary is thus a characteristic property of the set of differences $\mathcal{K}_d^1$.

3.2.3 Extension to Two Dimensions

To capture the bivariate case in (10), we extend these observations by a tensor product ansatz. To this end, we consider the function values of a function $g : \mathbb{R}^2 \to \mathbb{C}$ over the two-dimensional observation window $[0, q)^2$. Using the same relation $pq = 2\pi L$ established in (17), the function $\widehat{g}(\mathbf{k})$ is defined over the window $[0, p)^2$. The two windows in real and k-space are again sampled equidistantly by

$$
\begin{aligned}
\mathbf{x}_{j,l} &= \frac{q}{L}(j, l)^T, & g_{j,l} &= g(\mathbf{x}_{j,l}) \\
\mathbf{k}_{j,l} &= \frac{p}{L}(j, l)^T, & \widehat{g}_{j,l} &= \widehat{g}(\mathbf{k}_{j,l})
\end{aligned} \qquad \text{for} \quad j, l = 0, \ldots, L - 1. \qquad (28)
$$

The two-dimensional discrete Fourier transform is given by

$$
\widehat{g}_{j,l} := \frac{1}{L^2} \sum_{\mu,\nu=0}^{L-1} g_{\mu,\nu} \exp\left(-\frac{2\pi \mathrm{i}}{L} \langle (j, l)^T, (\mu, \nu)^T \rangle \right), \qquad j, l = 0, \ldots, L-1. \quad (29)
$$

As in the one-dimensional case, we shift the window in k-space such that it is symmetric around the origin. The definitions of minimal and maximal differences is generalized for elements $\mathbf{k}_j^d \in \mathcal{K}_d$, $j \in \mathcal{I}_d$ to the maximum norm according to

$$
k_{\min} := \min \left\{ \left\| \mathbf{k}_j^d - \mathbf{k}_l^d \right\|_\infty : j, l \in \mathcal{I}_d ; j \neq l \right\}, \qquad (30a)
$$

$$
k_{\max} := \max \left\{ \left\| \mathbf{k}_j^d - \mathbf{k}_l^d \right\|_\infty : j, l \in \mathcal{I}_d \right\}, \qquad (30b)
$$

and we again require (18), (26) and consequently (27).

The function to consider is of the form $g(\mathbf{x}) = c \exp(\mathrm{i}\langle \mathbf{k}, \mathbf{x} \rangle)$ and we again only know $\mathbf{k} \in \mathcal{K}_d$ and the values of the two-dimensional discrete Fourier transform $\widehat{g}_{j,l}$. We extend the one-dimensional strategy to get a reconstruction of the coefficient c. The amplitude and argument of c are now determined by the position of both the x and y components of $\mathbf{k}$ relative to the nearest grid points. This leads to four values which can to be utilized. Figure 3 illustrates one such tile. The four corner values $\widehat{g}_{mn} \in \mathbb{C}$, $m, n \in \{0, 1\}$, are indexed as

$$
\widehat{g}_{mn} := \widehat{g}_0\Big(\big((1 - m)\lfloor \mathbf{k}^x \rfloor + m\lceil \mathbf{k}^x \rceil\big) + \mathrm{i}\big((1 - n)\lfloor \mathbf{k}^y \rfloor + n\lceil \mathbf{k}^y \rceil\big)\Big). \qquad (31)
$$

The down and up brackets refer to the rounding operation to the next point on the Fourier grid. The scaled distances to the nearest coordinate axes in the second dimension are given analogously to (23) by

$$
d_0 := \frac{q}{2\pi}\tilde{d}_0, \qquad d_1 := \frac{q}{2\pi}\tilde{d}_1. \qquad (32)
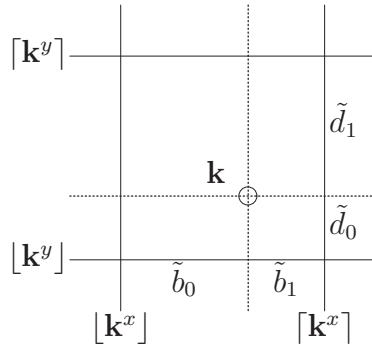$$

Fig. 3. A tile in two-dimensional Fourier space of width and height $pL^{-1} = 2\pi/q$ containing the fractional wave vector $\mathbf{k}$. $\tilde{b}_0 + \tilde{b}_1 = pL^{-1}$ and $\tilde{d}_0 + \tilde{d}_1 = pL^{-1}$ are the distances to the nearest coordinate lines in both directions.

The phase of the coefficient c is determined first. To this end, we extract a number $\tilde{c} \in \mathbb{C}$ called the *principal direction* according to the following rule:

$$\tilde{c} := \sum_{m,n=0}^{1} (-1)^{m+n} \widehat{g}_{mn} \,. \tag{33}$$

This averaging process is introduced here to compensate for errors as stated in Remark 3.3. The phase then follows from the difference between the angle of the direction and the predicted phase $\pi(b_0 + d_0)$ derived from (24):

$$\arg(c) = \arg(\tilde{c}) - \pi(b_0 + d_0) \,. \tag{34}$$

In the next step, each of the four corner values is used to find an equation for the modulus of c. We define

$$p_{mn} := (-1)^{m+n} \langle \widehat{g}_{mn}, \frac{\tilde{c}}{|\tilde{c}|} \rangle \,, \tag{35}$$

$$s_{mn} := \operatorname{sinc}(b_m) \operatorname{sinc}(d_n) \,. \tag{36}$$

The p_{mn} are the projections of the corner values onto the principal direction with a sign correction applied. The complex numbers $\widehat{g}_{mn}$ and $\tilde{c}$ in (35) have been interpreted as vectors in $\mathbb{R}^2 \sim \mathbb{C}$. The s_{mn} are the theoretical predictions for the amplitudes inferred from (25). The modulus ideally fulfills each of the four equations

$$|c| = \frac{p_{mn}}{s_{mn}}, \quad m,n \in \{0,1\} \,.$$

To account for perturbations, we interpret these equations as an over-determined problem. The optimal value for $|c|$ is derived through a straightforward least-squares ansatz leading to the formula

$$|c| := \left(\sum_{m,n=0}^{1} p_{mn} s_{mn} \right) \left(\sum_{m,n=0}^{1} s_{mn}^2 \right)^{-1} \,. \tag{37}$$
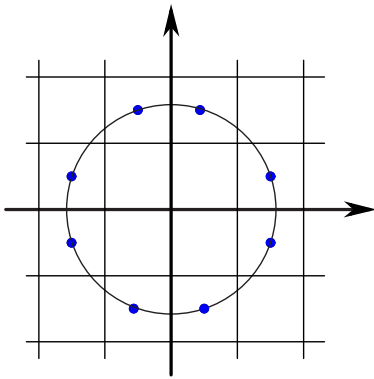
12

Fig. 4. Setup of wave vectors creating a periodic pattern.

This formula completes the derivation of the coefficient c from the values of $\widehat{g}$ at uniformly spaced grid points. We will use this procedure in Section 3.4 to find the coefficients of the plane wave basis functions.

3.3 Specialization to Periodic Patterns

The reconstruction of the coefficient of one single plane wave alone already requires a nontrivial computation. However, when the physical situation does not provide a-priori information about the directions of the wave vectors, this cannot be avoided.

Patterns arising from a random set of wave vectors are generally non-periodic, as the ratios of any two difference vectors most probably lead to irrational numbers. Therefore, the reconstruction can only be reasonably accurate inside the window of observation, and the quality deteriorates with increasing distance from it. In other words, the method described here performs a de-facto periodization of the target pattern restricted to the observation window.

In physical reality, periodic patterns are frequently needed, for example in the design of optical grids. Considering the principal difficulties mentioned before, it is reasonable to specialize to the case of periodic patterns. By a suitable adjustment of the length of the observation window, the need for subgrid approximation as detailed in the previous section disappears completely.

Periodic patterns are created when the projections of all differences of wave vectors onto the x-axis are in rational relation, and likewise for the y-axis. We write this as

$$\mathbf{k}_{j,l} \in k_{\min}\mathbb{Z}^2 \quad \text{for all } j, l \in \mathcal{I}. \tag{38}$$

As all wave vectors must have constant length K, the construction of an adequate setup is nontrivial. As has been outlined in [4], the general problem leads into the realm of number theory, but there are subclasses which can be easily identified. An example is shown in Figure 4.

We assume from now on that f_N fits into the observation window exactly once,

13

i. e., , it is a q-periodic function. This leads to the identity $q = \frac{2\pi}{k_{\min}}$. Provided that L is chosen large enough, cf. (26), the discrete Fourier transform $\widehat{f}_N$ can directly be evaluated at the points $\mathbf{k} \in \mathcal{K}_d$, and these values are at the same time the coefficients of the plane wave basis functions. They are assigned as follows,

$$
\widehat{f}_N(\mathbf{k}_{j,l}) = \begin{cases} c_j \bar{c}_l & \text{if } \mathbf{k}_{j,l} \in \mathcal{K}_{d,1} \\ c_j \bar{c}_l + c_m \bar{c}_n & \text{if } \mathbf{k}_{j,l} \in \mathcal{K}_{d,2} \\ \sum_{j=1}^{N} |c_j|^2 & \text{if } j = l \\ 0 & \text{else.} \end{cases}
\tag{39}
$$

Note that $j = l$ implies $\mathbf{k}_{j,l} = 0$. Reading these equations from right to left, we obtain a system of nonlinear equations, where the c_j are the unknowns and the values from the discrete Fourier transform constitute the right hand side, which is the discrete analogon of (12).

3.4 Determination of the Coefficients

The procedure developed in the previous sections can be interpreted as an approximation of a given function f by an element f_d from the linear space

$$
\mathcal{S}_d := \left\{ g \ : \ g = \sum_{\mathbf{k}_{j,l} \in \mathcal{K}_d} c_{j,l} \exp\big(\mathrm{i}\langle \cdot, \mathbf{k}_{j,l} \rangle\big); \ c_{j,l} \in \mathbb{C} \right\}.
\tag{40}
$$

The coefficients $c_{j,l}$ can be computed approximately by the approach in Section 3.2.3 for general beam setups, or directly by evaluation of the discrete Fourier transform for specific beam setups, as explained in Section 3.3. The choice of beam setup determines whether to employ the more general approximative method or the simpler method for periodic patterns

This means, that we are now equipped with the values

$$
c_{j,l} := \mathrm{eval}\left(\widehat{f}(\mathbf{k}_{j,l})\right), \ \text{if} \quad \mathbf{k}_{j,l} \in \mathcal{K}_{d,1}
\tag{41a}
$$

$$
\tilde{c}_{j,l} := \mathrm{eval}\left(\widehat{f}(\mathbf{k}_{j,l})\right), \ \text{if} \quad \mathbf{k}_{j,l} \in \mathcal{K}_{d,2},
\tag{41b}
$$

where the operator $\mathrm{eval}(\cdot)$ performs the approximative evaluation of the discrete Fourier transform between the grid points as described in previous section Section 3.3.

The computed function has the form

$$
f_d(\mathbf{x}) = \sum_{j=1}^{N} |c_j|^2 + \sum_{\mathbf{k}_{j,l} \in \mathcal{K}_{d,1}} \left(c_{j,l} \exp\big(\mathrm{i}\langle \mathbf{k}_{j,l}, \mathbf{x} \rangle\big) \right) + \sum_{\mathbf{k}_{j,l} \in \mathcal{K}_{d,2}} \left(\tilde{c}_{j,l} \exp\big(\mathrm{i}\langle \mathbf{k}_{j,l}, \mathbf{x} \rangle\big) \right).
\tag{42}
$$

14

However, the task in (4) was, to approximate from the nonlinear space

$$\mathcal{S}_N = \left\{ g = \left| \sum_{j=1}^N c_j \exp\left(i\langle \mathbf{k}_j, \, \cdot \,\rangle\right) \right|^2 \; : \; c_j \in \mathbb{C} \right\},$$

defined in (5). The next step is now to compute the approximation $f_* \in \mathcal{S}_N$ of $f_d \in \mathcal{S}_d$. Comparing the coefficients of f_N and f_d according to (10) and (42), we arrive at the following remark.

Remark 3.5 (The relation between $c_{j,l}$, $\tilde{c}_{j,l}$ and c_j). The values $c_{j,l}$ and $\tilde{c}_{j,l}$, which are known at this point comprise the right hand side of the nonlinear system of equations for the coefficients c_j, cf. (39). The determination of the c_j from the $c_{j,l}$ and $\tilde{c}_{j,l}$ according to the equations $c_j \bar{c}_l = c_{j,l}$ and $c_j \bar{c}_l + c_m \bar{c}_n = \tilde{c}_{j,l}$ is a highly over-determined problem.

To solve this problem, we collect all coefficients in a complex vector $\mathbf{c} := (c_1, \ldots, c_N)^T \in \mathbb{C}^N$ and denote by $\mathcal{I}_{d,e} \subset \mathbb{N} \times \mathbb{N}$ the index set of $\mathcal{K}_{d,e}$ for $e \in \{1, 2\}$. A generic least-squares ansatz leads to the definition of the cost functional

$$\mathcal{J}(\mathbf{c}) := \sum_{(j,l) \in \mathcal{I}_{d,1}} |c_j \bar{c}_l - c_{j,l}|^2 \quad + \sum_{(j,l) \in \mathcal{I}_{d,2}} |c_j \bar{c}_l + c_m \bar{c}_n - \tilde{c}_{j,l}|^2 \tag{43}$$

which we seek to minimize.

Remark 3.6 (Singular value decomposition). In case of linearly independent wave vectors, i.e., $\mathcal{K}_{d,2} = \emptyset$, the $c_{j,l}$ are the non-diagonal entries of a self-adjoint matrix $\mathbf{F}$. However, minimizing $\mathcal{J}$ is *not* equivalent to the minimization of $\|\mathbf{c}\mathbf{c}^* - \mathbf{F}\|_F^2$, which could be solved exactly by a singular value decomposition of $\mathbf{F}$. The equivalence is destroyed by the diagonal entries of $\mathbf{c}\mathbf{c}^*$, which do not appear in $\mathcal{J}$. Neither does it make sense to include it in the functional, as the diagonal contribution from (42) is of fundamentally different form.

A simple and efficient way to solve (43) is the *coordinate descent method* which minimizes the functional with respect to each complex direction separately. This strategy can be expressed by a sequence $\{\mathbf{c}^k\} \subset \mathbb{C}^N$ of complex valued vectors, defined by

$$c_j^{k+1} := \arg\min_{\xi \in \mathbb{C}} \mathcal{J}(c_1^{k+1}, \ldots, c_{j-1}^{k+1}, \xi, c_{j+1}^k, \ldots, c_N^k) \quad ; \quad j = 1, \ldots, N, \tag{44}$$

with any start vector $\mathbf{c}^0$. The index counter k identifies repeated rounds of one sweep over all coefficients.

The unique absolute minimum of $\mathcal{J}$ in the coordinate direction j_0 is given by

$$c_{j_0}^{\min} := \left(\sum_{\substack{(j,l) \in \mathcal{I}_{d,1} \\ j=j_0, l \neq j_0}} |c_j \bar{c}_l - c_{j,l}|^2 + \sum_{\substack{(j,l) \in \mathcal{I}_{d,2} \\ j=j_0, l \neq j_0}} |c_j \bar{c}_l + c_m \bar{c}_n - \tilde{c}_{j,l}|^2 \right) \left(\sum_{\substack{j=1 \\ j \neq j_0}}^{N} |c_j|^2 \right)^{-1} .$$
(45)

We have thus an explicit formula for the minimization in one coefficient alone. By minimizing for each coefficient in turn, we obtain a highly efficient numerical scheme. It can be shown [3] that the sequence $\{\mathbf{c}^k\}$ converges against a local minimum of $\mathcal{J}$. Implementing a straightforward choice of stopping criterion, we formulate the algorithm which computes a local solution of (44) as follows.

Algorithm 3.7. For a start value $\mathbf{c} \in \mathbb{C}^N$, an appropriate stopping parameter $\mu > 0$ and a maximum number of iterations $N_0 \in \mathbb{N}$ execute the following steps:

$$
\begin{aligned}
&m = 0 \\
&\mathcal{J}^m(g) := \mathcal{J}(c_1, \ldots, c_N) \\
&\textbf{do} \\
&\qquad \textbf{for } (j = 1, \ldots, N) \\
&\qquad\qquad c_j \leftarrow c_j^{min} \\
&\qquad \mathcal{J}^{m+1}(g) := \mathcal{J}(c_1, \ldots, c_N) \\
&\qquad m \leftarrow m + 1 \\
&\textbf{while } (\; |\mathcal{J}^m(g) - \mathcal{J}^{m-1}(g)| > \mu \quad \&\& \quad m < N_0 \;)
\end{aligned}
$$

We provide numerical results for selected patterns and beam numbers N in the next section. To verify our results obtained with the coordinate descend method, we have additionally employed the *Nelder and Mead simplex method* in the form of [3]. We will see below that our method yields results which are better than the simplex method in terms of human perception and in concrete error bounds.

4 Numerical Results

In this section, we will present numerical results addressing various aspects of the reconstruction. We tested the coordinate descent method for different beam setups, which cover both classes of beam vectors from Section 3.1 and a collection of target patterns.

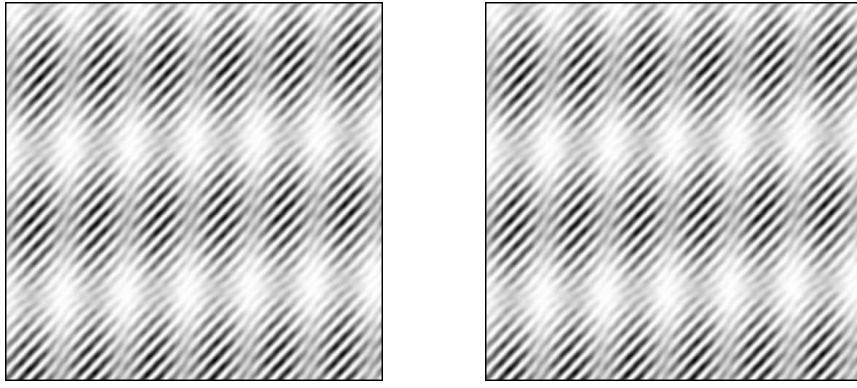The complete process of reconstruction for a given f is made up of three main

Fig. 5. Reconstruction of an image created with a randomly generated configuration ($N = 7$). The original image is shown on the left, the reconstruction on the right.

phases. This can be schematically written as

$$f \xrightarrow{(1)} \widehat{f} \xrightarrow{(2)} f_d \xrightarrow{(3)} f_* \,. \tag{46}$$

In the first step, the discrete Fourier transform is calculated. The second step excludes all values in k-space which do not belong to the set of beam differences $\mathcal{K}_d$. The last step employs the coordinate descent method which computes the appropriate values for the complex coefficients.

The following two sections will be slightly different in focus. First, we will discuss the quality of the general algorithm and provide examples which demonstrate its robustness against noise. In the second section, we will concentrate on the special case of periodic patterns. We will compare the results with the simplex method of Nelder and Mead, and provide additional tables where we examine the errors in the different steps of the reconstruction in detail.

4.1   General Setups of Beams

The first class of results deals with configurations of beams which have been generated randomly. As stated before, this gives rise to generally non-periodic patterns.

We begin with two examples, one with a small number of $N = 7$ beams, shown in Figure 5, and the other with a comparatively large number of $N = 101$ beams, see Figure 6. The beam directions have been chosen randomly, as well as the complex coefficients. Note that this implies that the random pattern is contained in $\mathcal{S}_N$. While indications of pseudo-periodicity can be recognized in the first case, this structure vanishes completely for 101 beams. For the human eye, the reconstruction generally appears to be very good in both cases. The resolution of finer structures survives even in the case of large N, although the contrast of the image is clearly reduced.

In a second series of experiments, we tested the robustness of our method
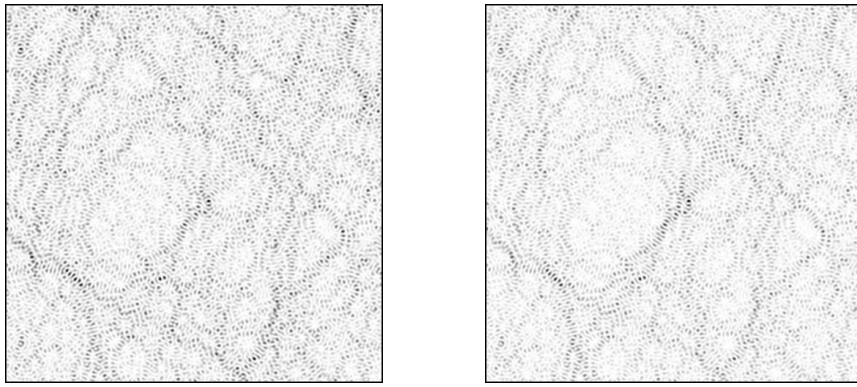
Fig. 6. Reconstruction of an image created with a randomly generated configuration ($N = 101$).
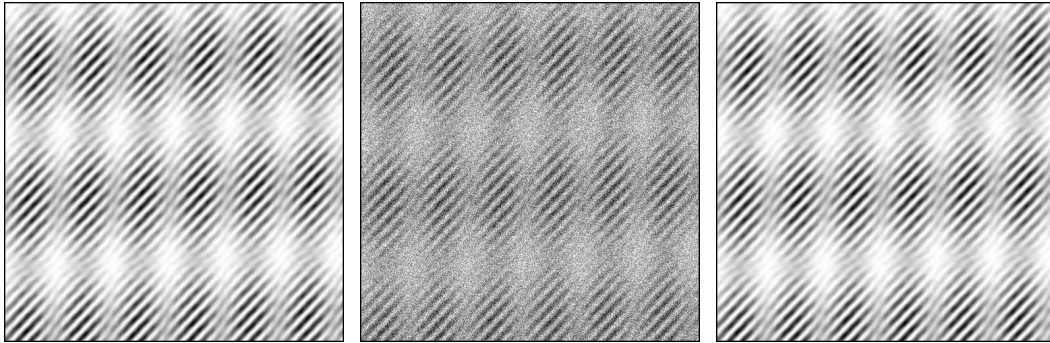

Fig. 7. These images demonstrate the robustness against random noise for the case $N = 7$. The original image is shown on the left, the state after the application of noise can be seen in the middle, and the reconstructed image is displayed on the right.
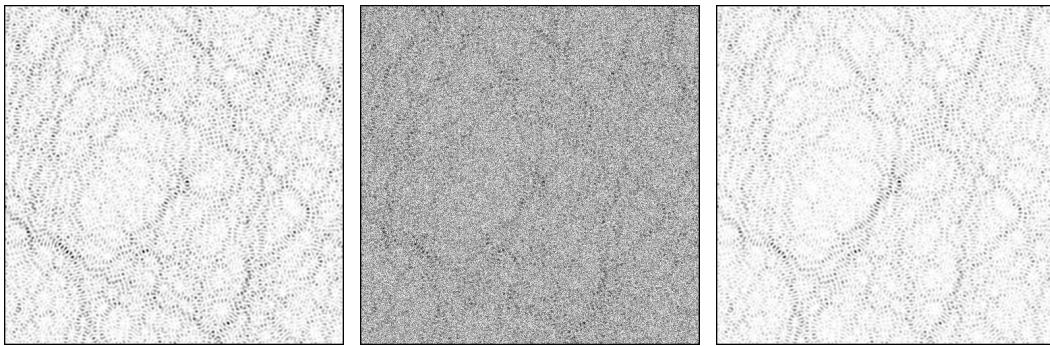

Fig. 8. We show a repetition of the above procedure for the case $N = 101$.

of reconstruction with noisy data. To this end, we added white noise to the original image before applying the algorithm. Without any modifications, the noise was filtered out completely, as can be seen in Figure 7 and Figure 8. An explanation of this behavior can be given based on Fourier analysis: the Fourier spectrum of white noise is concentrated at the origin and, consequently, the value $\widehat{f}(0)$ is modified, while all other Fourier coefficients are not changed significantly. Reviewing (43) and (41a), we see that $\widehat{f}(0)$ does not occur on
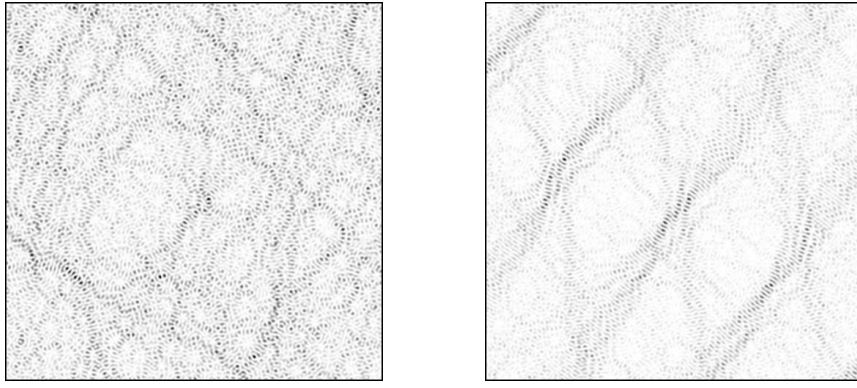
Fig. 9. We display the original image with $N = 101$, created from a random configuration of beams, and its reconstruction using an equidistant beam setup with the same number of beams.
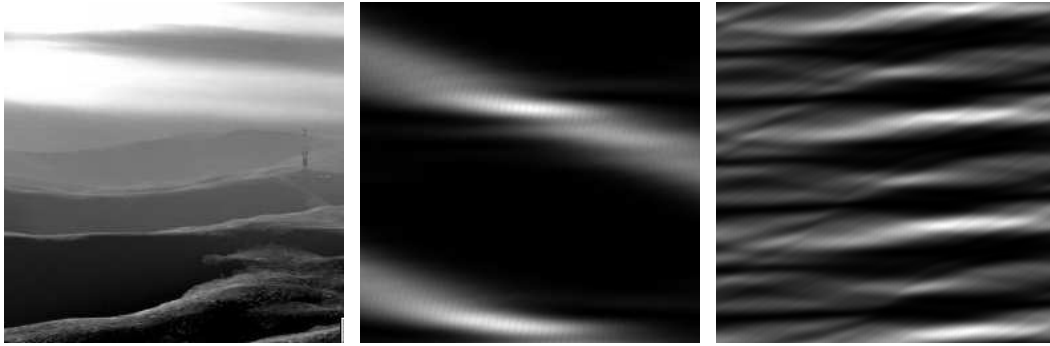

Fig. 10. A photographic image (of dimensions 256×256) "reconstructed" with wave lengths of 10 and 5 pixels, respectively, using an equidistant setup of $N = 101$ beams.

the right hand side of the nonlinear system of equations.

The last point which we wish to make in this section deals with the importance of matching beam differences. We tried to reconstruct the random configuration from Figure 6 with a different setup of beams. To this end, we used 101 beams which were equidistantly distributed around the circle. We chose an odd number because this leads to a linearly independent set of beam differences. Regarding the results in Figure 9, we must say that the reconstruction with a different beam setup fails completely. We can see that the structures on the small scales conserve their character, while no similarity survives on the global scale. This is however not surprising, as the entries in Fourier space of both distributions of beam differences generally do not have many common points. We demonstrate in Figure 10 that it is even more beyond the capabilities of our algorithm to reconstruct arbitrary images, such as photographs. Besides purely imaginary resemblances, the image is clearly outside the class of reconstructible patterns. This is caused by the principal discrepancy between the set $\mathcal{K}_\mathrm{d}$ of reachable differences in Fourier space and the set of Fourier values of large amplitude in the original picture.

19

In view of the observation that the class of reconstructible patterns is rather limited, we now choose the target pattern outside of the set $\mathcal{S}_N$, but with a simple structure, and turn our point of interest to periodic beam setups. As already stated in Section 3.3, the choice of such setups renders the approximative calculation of the coefficients $c_{j,l}$ and $\tilde{c}_{j,l}$ in (42) unnecessary. They can directly be derived from the discrete Fourier transform, namely by taking its values at the appropriate elements $\mathbf{k} \in \mathcal{K}_\mathrm{d}$ according to (39). By choosing the norm

$$\|f\|_\Omega \;:=\; \|f\|_{\ell_2} := \sqrt{\sum_{j,\,l=0}^{L-1} \left| \widehat{f}_{j,l} \right|^2}$$

for any grid size L of the discrete Fourier transform, f_d is the best approximation from $\mathcal{S}_\mathrm{d}$ to the given function $f \notin \mathcal{S}_\mathrm{d}$. The only numerical approximation therefore needs to be performed in step (3) of the reconstruction (46). This is done by an application of the coordinate descent method in order to minimize the cost functional $\mathcal{J}$ from (43). As already mentioned, the *Nelder and Mead simplex method* was also applied to minimize the cost functional. A comparison of the results of both methods below shows the good performance of the coordinate descend method and demonstrate that it is well suited for this type of optimization problem.

In order to compare the influences of the a priori choice of beam setup, we reconstruct three different images of a simple structure with two beam setups, each with a different number of beams. The resolution of the discrete Fourier transform has been fixed at $L = 256$. The resolution of the images is in all cases set to 256×256 pixels. Their intensity values range from 0.0 (black) to 1.0 (white).

The first applied beam setup consists of eight beams, located such that their differences, i.e., the elements $\mathbf{k} \in \mathcal{K}_\mathrm{d}$, all lie on grid points close to the origin. This seems to be a reasonable choice, as the most important Fourier coefficients of a typical image appear at low frequencies. Recall that the failure of reconstruction of arbitrary patterns in Section 4.2 was explained by the fact that the entries in Fourier space of the beam differences and the given pattern had no common points. Hence, one expects here at least the coincidence of the most significant points in Fourier space. The positions of the wave vectors and their differences are shown in Figure 11, Figure 13 and Figure 14 show the original image as well as the approximations f_d and f_*, reconstructed once with the coordinate descent method and with the Nelder and Mead simplex method. These graphics as well as all subsequent ones always display the results in the same order. For periodic setups, the linear approximation f_d depends only on the choice of the beam setup. All linear approximations attain the structure of the original image, which permits to state that these
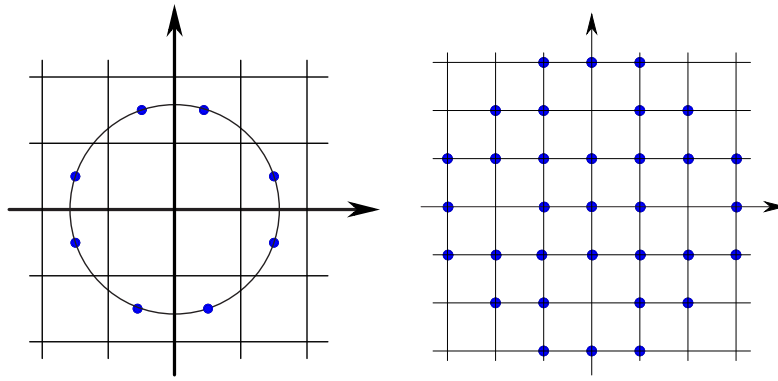
Fig. 11. A beam setup, with eight wave vectors $\mathbf{k}_j \in \mathcal{K}$ for a periodic setup. The resulting differences in $\mathcal{K}_{\mathrm{d}}$ with $k_{\min} = \frac{2K}{\sqrt{10}}$ are shown in the right image.
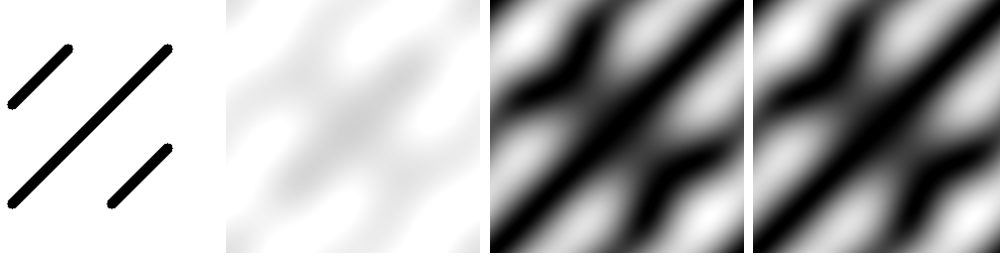

Fig. 12. A simple structure, that was reconstructed by the set $\mathcal{K}$, as it is sketched in Figure 11. The two left images show the original structure f (leftmost) and its best approximation f_d from $\mathcal{S}_d$. On the right, two nonlinear approximations $f_* \in \mathcal{S}_N$ are displayed which were calculated by the Nelder and Mead simplex method (rightmost) and the coordinate descent method.
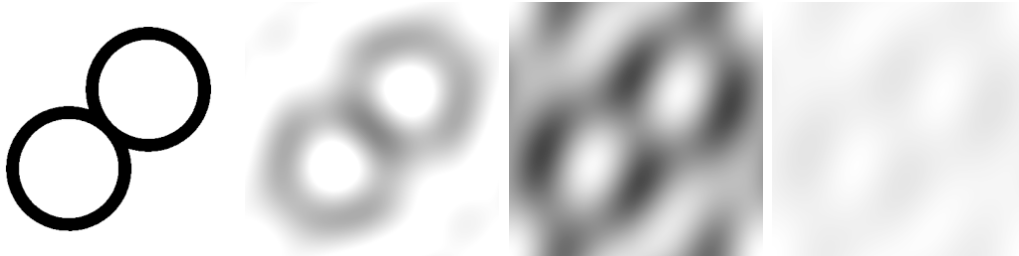
Fig. 13. Here, a different structure was reconstructed. The displayed order is again from left to right: original structure f, best approximation f_d, nonlinear approximations f_* calculated by the coordinate descent method and the Nelder and Mead simplex method.

eight beams form an appropriate setup for the reconstruction. The nonlinear approximations $f_* \in \mathcal{S}_N$ also reconstruct the structure of the respective f_{d} for both numerical methods. In fact, the results of the methods differ only in intensity, not in structure. The structure of the letter "S" is preserved well. Here, both iteration schemes deliver almost the same visual result. We conclude that the reconstructions are satisfactory and the performances of the iteration schemes are of the same quality in all cases.
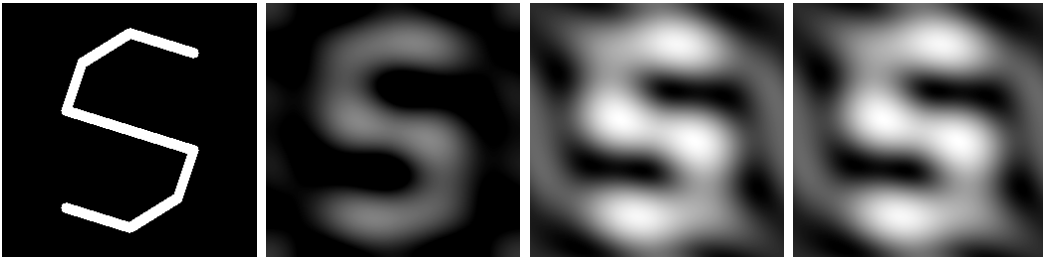
Fig. 14. One more reconstruction with the periodic setup from Figure 11. The images are ordered as in Figure 12 and Figure 13.
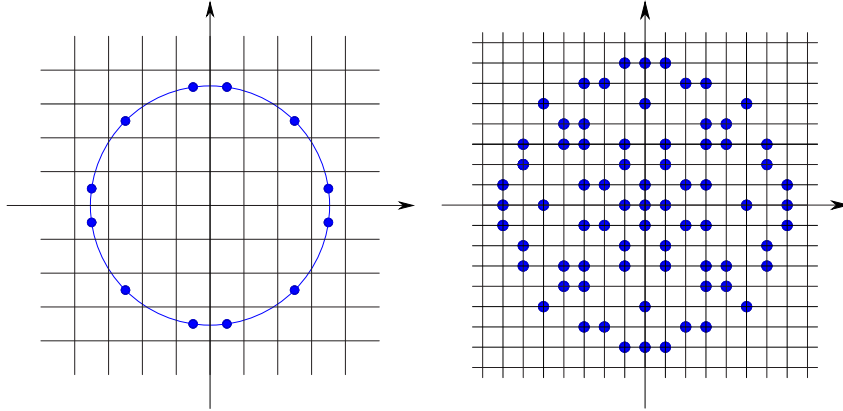

Fig. 15. An alternative periodic beam setup with twelve laser beams (left image). For $k_{\min} = \frac{2K}{\sqrt{50}}$ all elements in $\mathcal{K}_d$ lie on the grid in Fourier space, as shown in the right image. The period of f_N is $q = \frac{\sqrt{50}}{K}\pi$.

The good results of the approximation with eight beams motivate an extension of the number of beams. To ensure that we can still achieve differences on the grid, i.e., that we obtain in a periodic setup, twelve beams are suitably arranged. Figure 15 shows the distribution of the wave vectors on the circle. The resulting differences are now partly located close to the origin, and partly separated by a considerable distance. One can see directly the relation $\mathcal{K}_d \ni \mathbf{k} = k_{\min}\mathbb{Z}^2$ for periodic setups from Section 3.3. Thus f_N is a periodic function with period $q = \frac{\sqrt{10}}{K}\pi$. The sets $\mathcal{K}_{d,1}$ and $\mathcal{K}_{d,2}$ are both not empty. This leads to gaps in the distribution of the $\mathbf{k} \in \mathcal{K}_d$ on the grid. Altogether the grid points directly around the origin are not as densely occupied as in the setup with eight beams from Figure 11.

In order to compare the influence of the choice of beam setup, we consider the same examples as treated previously with eight beams. The results are shown in Figure 16, Figure 17 and Figure 18.

Although we have increased the number of beams and hence the number of beam differences, the results are now inferior in quality. The linear approximations $f_d \in \mathcal{S}_d$ in Figure 16 and Figure 17 show some similarities in the raw structure, however, no detailed reconstruction could be achieved. This is due to the characteristics of the beam setup. We reason that f_d is a linear
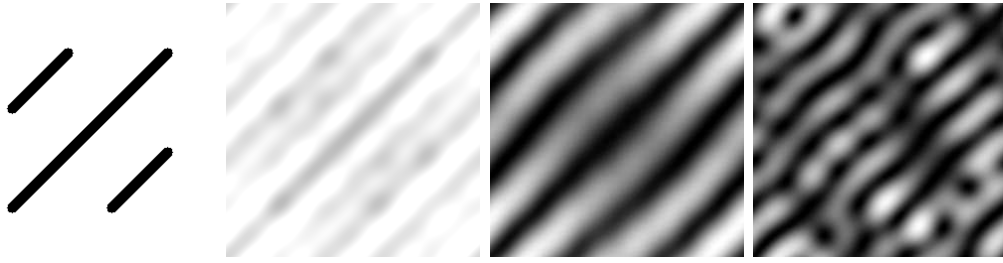
22

Fig. 16. The original image is the same as in Figure 12, however this image is reconstructed with the beam setup from Figure 15. The images show from left to right the original image, the best approximation f_d for this setup and the reconstruction of f_* with the coordinate descent method respectively with the Nelder and Mead simplex method (rightmost).
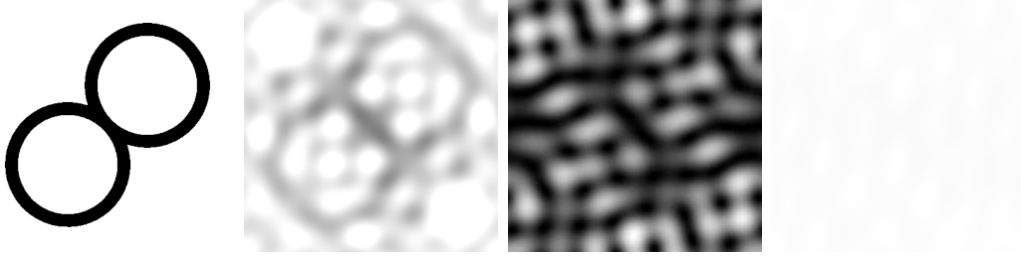

Fig. 17. In this reconstruction with the setup from Figure 15, a likewise effect occurs as in Figure 16. The displayed order is again from left to right: f, f_d and f_* calculated with the coordinate descent method and the Nelder and Mead simplex method.
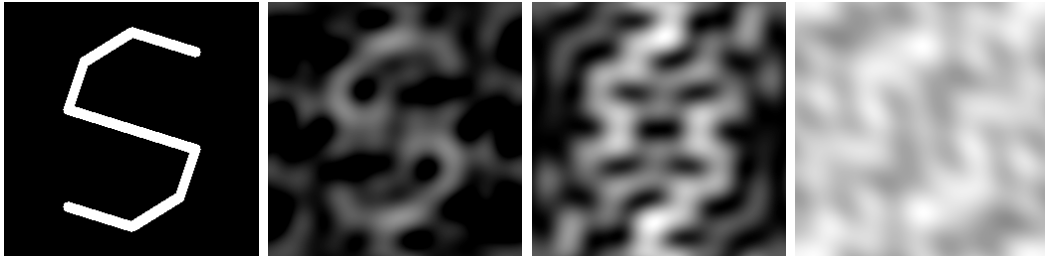

Fig. 18. Here, the beam setup from Figure 15 is applied to the same image as in Figure 14. The images are ordered as in all previous figures.

combination of plane waves with wave vectors $\mathbf{k} \in \mathcal{K}_\mathrm{d}$. If too few elements $\mathbf{k} \in \mathcal{K}_\mathrm{d}$ are located close to the origin, the lower frequencies are badly represented. In addition to that, the gaps in the distribution of differences and the lack of these frequencies in the spectrum of f_d cause the poor reconstructions. As a further consequence of these poor reconstructions f_d, the final nonlinear approximations $f_* \in \mathcal{S}_N$ are unsatisfactory.

The computed results for the two setups show the performance of the numerical iteration methods applied to the minimization of the cost functional, i.e., the calculation of the nonlinear approximations f_*. The results for the first eight-beam setup (Figure 11) are all very similar for both methods. They only differ in the intensity of the created image, However, as the cost functional

ignores any reference to the average intensity of the image, this is no valid criterion concerning the quality of any method. For the second twelve-beam setup (Figure 15) this is different. Here, the results of the coordinate descend method and of the Nelder and Mead simplex method do not only differ in intensity, but also in the structure of the reconstructions. For this setup, the results of the simplex method are inferior to those of the coordinate descend method, in the sense that the reconstructions with the latter method show more similarities to the respective f_d than the first. The result $f_* \in \mathcal{S}_N$ of the coordinate descend method could attain the raw structure of f_d, while the Nelder and Mead simplex method failed in that task. In general, the reconstruction is, even for the numerically better method, not satisfactory. The approximation $f_d \in \mathcal{S}_d$ achieves the main structure of the original image, but also shows some additional artifacts. This function is shown next to the original image on the left. The final approximations $f_* \in \mathcal{S}_N$, shown in the images on the right (same order as in previous images), have no more similarity to the original image. The Nelder and Mead simplex method delivers a very "bright" result, such that no more structure is recognizable. As for the last reconstruction example, though the linear approximation $f_d \in \mathcal{S}_d$ shows again some little artifacts, it can be taken as a very good first approximation. This good approximation f_d could, however, not be approximated well by the respective final nonlinear approximations $f_* \in \mathcal{S}_N$ for both methods. The original structure becomes completely lost in this numerical reconstruction step.

5   Conclusion

In this article we presented a method for the calculation of beam coefficients from a given target pattern. The coefficients represent the phases and amplitudes for the individual beams of a given laser setup. The directions of the beams have been considered as fixed parameters of the problem.

The initial mathematical model has been investigated by means of Fourier analysis. The nonlinear approximation space $\mathcal{S}_N$ gives rise to an overdetermined system of nonlinear equations for the complex-valued coefficients.

The right hand side of this system is derived from the expansion coefficients of the best approximation from a linear space $\mathcal{S}_d$, which is spanned by the basis functions occurring already in the definition of the nonlinear space $\mathcal{S}_N$. This basis consists of plane wave functions, whose coefficients can be directly identified as the values of the Fourier transform of the pattern at specific points in Fourier space determined by the mutual differences of beam directions. For a numerical solution of the problem, the continuous Fourier transform needs to be replaced by the discrete Fourier transform. A minimum resolution of the discrete Fourier transform depending on the given wave vectors can be derived based on the characteristics of the beam setup. As the beam differences

in general do not lie on the discrete Fourier grid, the values at intermediate points have to be derived from their neighbours on the grid. A method was proposed to interpolate the coefficients from the values of the discrete Fourier transform on the grid.

Turning to a special subclass of beam setups that give rise to periodic patterns, we showed that the grid can be scaled in such a manner that all desired coefficients are delivered directly by the discrete Fourier transform.

To solve the over-determined system of nonlinear equations, we minimized a cost functional by applying a coordinate descend method. Additionally, the general Nelder and Mead simplex method was applied in the periodic case. In general, we can say that our method delivered good results in all cases which we examined, as it reconstructs only the best approximation from the linear space $\mathcal{S}_d$, which is the right hand side of the cost functional. Therefore, this best approximation is the optimal result that can be achieved in any case and the quality of the complete process of reconstruction is determined by the distance of the Fourier transformation of the target pattern to the space $\mathcal{S}_\mathrm{d}$.

Thus, the quality of reconstruction is principally determined by the choice of an appropriate setup for any given pattern. This can be reconstructed well only if the most significant Fourier coefficients of the pattern are captured by the differences of beam directions from the setup. In this case which arises, in particular, when the pattern f lies in $\mathcal{S}_N$, the reconstruction is good. However, in the general case that $f \notin \mathcal{S}_N$, the beam setup should meet most of the significant Fourier coefficients which are usually located close to the origin, to produce an acceptable image. This explains why the setup with $N = 8$ beams proves superior to the setup with 12 beams.

Of course, the quality of the reconstructions would be improved further if we could formulate an algorithm to automatically choose beam setups $\mathcal{K}_d$ of relatively large N, which are densely populated near the origin and are ideally matched to the characteristics of the target image in Fourier space. This, however, leads to the problem to approximate an object from an extremely complicated nonlinear space for which it is likely that concepts from number theory and combinatorial optimization would come into play. As mathematical results are not yet available, the development of deterministic algorithms with reasonable complexity for the most general problem are currently out of reach.

Acknowledgments

References

[1] W. R. Anderson, C. C. Bradley, J. J. McClelland, and R. J. Celotta. Minimizing feature width in atom optically fabricated chromium nanostructures. *Phys. Rev. A* 59, 3:2476-2485, 1999.

[2] A. S. Bell, B. Brezger, U. Drodofsky, S. Nowak, T. Pfau, J. Stuhler, Th. Schulze, and J. Mlynek. Nano-lithography with atoms. *Surf. Sci.*, 433-435:40–47, 1999.

[3] D. P. Bertsekas. *Nonlinear Programming.* Athena Scientific, 2nd edition, 1999.

[4] J. Braun. Numerische Berechnung von komplexen Lichtmasken zur atomaren Nanofabrikation. Diploma Thesis, Universität Bonn, 2004.

[5] R. Courant and D. Hilbert. *Methods of Mathematical Physics. Volume II: Partial differential equations.* Wiley Classics Edition (John Wiley & Sons/Interscience Publishers), 1989.

[6] F. John. *Plane waves and spherical means. Applied to partial differential equations.* Springer-Verlag, New York – Heidelberg – Berlin, 1981.

[7] C. Keller, J. Schmiedmayer, and A. Zeilinger. Requirements for coherent atom channeling. *Optics Communications* 179: 129–135, 2000.

[8] B. S. Logan and L. A. Shepp. Optimal reconstruction of a function from its projections. *Duke Math. J.*, 42:645–659, 1975.

[9] H. J. Metcalf and P. v. d. Straten. *Laser Cooling and Trapping.* Springer-Verlag, Heidelberg, 1999.

[10] M. Mützel, D. Haubrich, D. Meschede, K. Peithmann, M. Flaspöhler, and K. Buse. Atom lithography with a holographic light mask. *Phys. Rev. Lett.*, 88:8, 2002.

[11] D. Meschede and H. Metcalf. Atomic nanofabrication: atomic deposition and lithography by laser and magnetic forces. *J. Phys.*, D 36:R17-R38, 2003.

[12] M. Mützel, U. Rasbach, D. Meschede, C. Burstedde, J. Braun, A. Kunoth, K. Peithmann, and K. Buse. Atomic nanofabrication with complex light fields. *Appl. Phys.*, B 77:1–9, 2003.

[13] A. Pinkus. Approximation by ridge functions, *in*: Surface Fitting and Multiresolution Methods. *Vanderbilt University Press, Nashville, TN*, pages 279–292, 1997.

[14] S. Stenholm. Laser cooling and trapping. *Eur. J. Phys* 9: 242–249, 1988.

[15] J. H. Thywissen, K. S. Johnson, R. Younkin, N. H. Dekker, K. K. Berggren, A. P. Chu, M. Prentiss, and S. A. Lee. Nanofabrication using neutral atomic beams. *J. Vac. Sci. Technol. B*, 15:6, 1997.